This is an *Accepted Manuscript*, which has been through the Royal Society of Chemistry peer review process and has been accepted for publication.

Accepted Manuscripts are published online shortly after acceptance, before technical editing, formatting and proof reading. Using this free service, authors can make their results available to the community, in citable form, before we publish the edited article. We will replace this *Accepted Manuscript* with the edited and formatted *Advance Article* as soon as it is available.

You can find more information about *Accepted Manuscripts* in the **Information for Authors**.

Please note that technical editing may introduce minor changes to the text and/or graphics, which may alter content. The journal's standard **Terms & Conditions** and the **Ethical guidelines** still apply. In no event shall the Royal Society of Chemistry be held responsible for any errors or omissions in this *Accepted Manuscript* or any consequences arising from the use of any information it contains.

Journal Name

ARTICLE

Surfactant-Free Green Synthesis of Fe_3O_4 Nanoparticles capped with 3,4-Dihydroxyphenethylcarbamodithioate: Stable Recyclable Magnetic Nanoparticles for Rapid and Efficient Removal of Hg(II) Ions from Water

Sada Venkateswarlu and Minyoung Yoon*

Mercury is considered as one of the most notorious global pollutants due to its high toxicity and widespread use in industry. Although many materials have been developed for the removal of mercury for water purification, most of these materials are difficult to reuse, which may lead to an increase in the mercury handling expense. Therefore, new sustainable materials that can be easily recycled and are highly efficient for removal of mercury are required. Herein, we report the surfatant-free green synthesis of Fe_3O_4 magnetic nanoparticles (MNPs) using watermelon (*Citrullus lanatus*) rind extract. The Fe_3O_4 MNPs were further functionalized with 3,4-dihydroxyphenethylcarbamodithioate (DHPCT) and applied to the removal of Hg(II). Evaluation of the mercury removal efficiency and adsorbed amount by the DHPCT@Fe_3O_4 MNPs demonstrated the high Hg(II) removal efficiency (98%) with a maximum Hg(II) adsorption capacity of 52.1 mg/g. The systematic studies of the adsorption mechanism, and selectivity suggests that the soft ligand (DHPCT) that can preferentially coordinate with the soft metal ion (Hg(II)) resulting in the selective mercury removal. The developed DHPCT@Fe_3O_4 MNPs were readily recycled several times using an external magnet by exploiting their ferromagnetic character, without a significant decline in the Hg(II) removal efficiency. This study provides a new insight into the preparation of a highly efficient adsorbent for Hg(II) removal by an eco-friendly method.

1. Introduction

Owing to rapid industrial growth, the increasing discharge of toxic heavy metals into the environment in wastewater has become a cause of serious water pollution.[1,2] Among the various heavy metal ions, mercury is considered as one of the most notorious global pollutants due to its high toxicity and widespread industrial use in fields such as the manufacture of electrical and electronic components, fossil fuel combustion, halogen and alkali metal preparation, sulfide ore roasting operations, and battery industries.[3-5] Intake of even low concentrations of mercury can damage vital organs, such as the lung, heart, kidney and brain.[6-7] Due to its solubility and stability, divalent Hg is the common inorganic form of mercury in both anthropogenic effluents as well as in the aquatic environment. Divalent mercury may be converted into more toxic organometallic forms *via* biological methylation.[8] The concentration limit of Hg(II) in drinking water established by the Environmental Protection Agency (EPA) is 0.002 mg/L. Therefore, it is imperative to develop efficient techniques for removal of Hg(II) from water. Although traditional methods for removing mercury species from water including chemical

precipitation, amalgamation, electro-deposition, ion exchange, reverse osmosis, membrane filtration, and photo-reduction have developed,[9-12] most of the conventional methods are costly, inefficient, and/or time-consuming. However, the adsorption process is recognized as the most promising approach for wastewater treatment because of its significant advantages, including the low-cost of materials, availability, ease of operation, and high-efficiency in comparison with other conventional methods. Even though various adsorbents have shown high efficiency for removal of mercury,[13-18] their widespread application has been curtailed by drawbacks such as the sophisticated synthetic procedures and the requirement for further recovery by centrifugation or filtration.

Recently, the application of nanomaterials in environmental remediation and pollutant removal has become an area of focus due to the exceptional properties of these materials, such as their high surface area, excellent absorption capacity, and easy functionalizability.[19-21] In addition, nanomaterials can scan a large volume of solvent in a short time due to very fast Brownian motion. Among the many types of nanomaterials, magnetic nanomaterials exhibit superior properties derived from their magnetic behavior; these materials can be easily and rapidly isolated from sample solutions by application of an external magnet without the requirement for further isolation process such as centrifugation or filtration.[22] Moreover, magnetite nanoparticles have earned distinction due to their

a. *Department of Nanochemistry, College of Bionano, Gachon University, Sungnam, 13120, Republic of Korea. E-mail: myyoon@gachon.ac.kr*

novel physicochemical properties; these materials have found utility in a large variety of applications, including in magnetic storage media,[23] targeted drug delivery,[24] catalysis,[25] MRI contrast agents,[26] environmental separation process,[27-29] and DNA extraction.[30] Magnetite nanoparticles have been prepared *via* various techniques, including microwave-assisted[31] and sonochemical methods,[32] the polyol route,[33] hydrothermal processes,[34] and chemical co-precipitation.[35] However, most of the reported processes require the use of an organic solvent such as benzene or hydrazine; such solvents are highly reactive and are potentially hazardous to the environment. To overcome the drawbacks of the reported synthetic processes, such as the environmentally unfriendly, expensive, and time-consuming nature, the development of environmentally benign and cheap synthetic methods remains a challenging objective. Only a few green synthetic methods utilizing bio-waste materials have been reported for production of Fe_3O_4.[36,37] Among a variety of biogenic sources, watermelon rind waste can draw attentions because South Korea is the eighth largest watermelon producing country in the world.[38] Although watermelon is a rich source of polyphenols, citrulline (amino acid), cellulose (carbohydrate), and carotenoids,[39,40] which can function as reducing and capping agents in the synthesis of Fe_3O_4 magnetic nanoparticles (MNPs), only a few studies have focused on utilization of these rinds.[41,42]

Herein, we present the facile synthesis Fe_3O_4 nanoparticles using an abundantly available waste, watermelon rind extract without using a chemical surfactant and reducing agent. The biogenic Fe_3O_4 nanoparticles were further functionalized by a 3,4-dihydroxyphenethylcarbamodithioate (DHPCT) ligand for an application of heavy metal ion (mercury) removal. Based on the hard and soft acid-base principle,[43] mercury is a soft acid and preferentially forms coordination complex with a soft base (e.g., sulfide or thiosulfate ions) in the DHPCT ligand.[44] Using the DHPCT@Fe_3O_4 MNPs, herein, we evaluate the optimum adsorption conditions, adsorption isotherms, and kinetics of Hg(II) removal by these species. The facile recyclability of the material is also demonstrated.

2. Experimental

2.1 Materials

Ferric chloride hexahydrate ($FeCl_3·6H_2O$), sodium acetate (CH_3COONa), HNO_3, $NaOH$, dopamine hydrochloride, carbon disulfide, and mercury nitrate monohydrate ($Hg(NO_3)_2·H_2O$) were purchased from Sigma Aldrich and Samchun Chemical. Watermelons were collected from a local market in Sujeong-gu, Sungnam, Gyeonggi-do, South Korea. Deionized Millipore water was used to prepare all solutions.
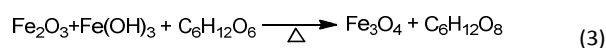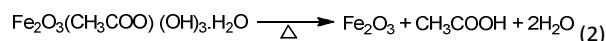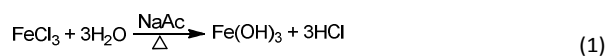
2.2 Extraction of watermelon rind

The collected rinds were thoroughly rinsed with deionized water to remove dust particles. The watermelon rinds were cut into small pieces and shade dried at room temperature for about 21 days under dust free conditions. The dried rind

pieces (15 g) were blended with 100 ml of water in a 250 ml round-bottom flask and refluxed for 1 h at 70 °C until the color of the aqueous solution changed to light yellow. The resulting mixture was cooled to room temperature and filtered with cheesecloth. The filtrate was stored at −4 °C in a refrigerator for further experiments.

2.3 Synthesis of DHPCT@Fe_3O_4 MNPs

The protocol for synthesis of the Fe_3O_4 MNPs without a reducing agent involved dissolving $FeCl_3·6H_2O$ (1.08 g, 4 mmol) and sodium acetate (3.28 g, 40 mmol) in 40 ml of freshly prepared watermelon rind extract solution with vigorous stirring for 2 h at 80 °C in a 100 ml round-bottom flask. The reaction mixture assumed a homogenous black color after 2 h. Sodium acetate can provide elemental oxygen for the formation of Fe_3O_4 and the extract solution acts as a reducing and capping agent. The obtained black product was isolated by applying an external magnetic field. The product was washed three times with ethanol, then with water, followed by drying in a vacuum oven at 95 °C overnight. We found that if the watermelon rind extract is further diluted by additional solvent, Fe_3O_4 MNPs can be reproducibly prepared regardless of batch of watermelon rind extract (See ESI). The procedure for synthesis of DHPCT is shown in Scheme 1. To attach DHPCT on the Fe_3O_4 MNPs, the dried Fe_3O_4 MNPs (0.463 g), DHPCT (0.0529 g), and deionized water (20 ml) were mixed in a 50 ml round-bottom flask and sonicated for 10 h at room temperature; the pH was then adjusted by addition of 0.1 M NaOH solution (pH 9). The DHPCT-capped Fe_3O_4 MNPs were separated by applying an external magnetic field, washed thoroughly with ethanol and deionized water for three cycles, and finally dried at 95 °C under dynamic vacuum to yield the DHPCT@Fe_3O_4 MNPs.

$$FeCl_3 + 3H_2O \xrightarrow[\triangle]{NaAc} Fe(OH)_3 + 3HCl \tag{1}$$

$$Fe_2O_3(CH_3COO)(OH)_3·H_2O \xrightarrow{\triangle} Fe_2O_3 + CH_3COOH + 2H_2O \tag{2}$$

$$Fe_2O_3 + Fe(OH)_3 + C_6H_{12}O_6 \xrightarrow{\triangle} Fe_3O_4 + C_6H_{12}O_8 \tag{3}$$

$$Fe_3O_4 + DHPCT \xrightarrow{\triangle} DHPCT@Fe_3O_4 \tag{4}$$

In the typical synthesis process, watermelon rind extract solution containing carbohydrates and polyphenols may play the role of a reducing agent. Sodium acetate acts as an electrostatic stabilizing agent and also as a ligand to form an intermediate complex phase iron oxide acetate hydroxide hydrate (Eq. 1). Although Fe_2O_3 may also be formed (Eq. 2), as observed in previous reports,[45] the generated Fe_2O_3 can be further transformed into Fe_3O_4 MNPs with the assistance of the carbohydrates present in the watermelon rind extract (Eq. 3). Finally, DHPCT can be incorporated on the surface of the Fe_3O_4 MNPs in alkaline medium.

2.4 Characterization

The crystalline phase and structure of the Fe_3O_4 MNPs were analyzed by using a X-ray diffractometer (Rigaku Ultima III

system) equipped with a Cu sealed tube (λ = 1.54178 Å) under the following conditions: 40 kV, 30 mA, increment = 0.05°, scan speed = 3 deg/min. The inverse spinel structure of Fe_3O_4 was also characterized using a PHIZuantera II X-ray photoelectron spectrometer (XPS). The morphology and size distribution of the Fe_3O_4 magnetic nanoparticles were determined *via* transmission electron microscope (TEM) images recorded with a Tecnai G2 transmission electron microscope, using an accelerating voltage of 300 kV; the composition of the resulting products was evaluated by using an EDAX analyzer (DPP-II) to acquire the energy dispersive spectrum (EDS). The magnetization loops for the magnetite nanoparticles washed with ethanol were measured at room temperature using a vibrating sample magnetometer (VSM, LKSM-7410). The specific surface area and pore diameter were analyzed using a Micromeritics ASAP-2020 instrument. High purity gases (99.999%) were used for the measurements. Fourier transform infrared (FT-IR) analysis of the watermelon rind extract and the synthesized materials was performed using a JASCO FTIR-4600 instrument and the iron oxide phase was evaluated by using a LABRAM HR 800 micro-Raman spectrometer. Thermal gravimetric analysis (TGA) was carried out using a Linseis L81-I TG-DTA instrument; the heating rate was set to 10 °C min^{-1} and measurements were performed under N_2 atmosphere.

2.5 Batch adsorption studies

The adsorption of Hg(II) on the DHPCT@Fe_3O_4 nano-composite was investigated in aqueous solution using batch adsorption experiments within the pH range of 2 to 9, at 303 K. Stock solution of Hg(II) (1000 mg L^{-1}) was prepared by dissolving required amount of a mercury salt in deionized Millipore water and diluted to get solutions of desired concentrations. The prepared magnetic nano-adsorbent (2.5 mg) was added to 25 ml of each Hg(II) ion solution. The initial pH of the Hg(II) solution was adjusted by using 0.1 M HNO_3 or 0.1 M NaOH solution. The solution mixture was ultrasonicated at room temperature for 5 min and transferred to a 100 ml Erlenmeyer flask, followed by shaking in a thermostatic incubator (200 rpm) at 303 K. The magnetic nano-adsorbent was removed from the solution using a permanent magnet. The concentration of Hg(II) ions was determined using flame atomic absorption spectroscopy (FAAS; Shimadzu AA–6300). For evaluation of the effect of pH, the loading of the DHPCT@Fe_3O_4 MNPs was kept constant at 0.10 g/L. The adsorption experiment was repeated in triplicate. The amount of Hg(II) adsorbed by the magnetic nano-adsorbent at equilibrium was calculated using Eq. 5. The percentage of mercury ions adsorbed was calculated using Eq. 6.

$$q_e = \frac{(C_i - C_e)V}{M} \qquad (5)$$

$$Adsorption(\%) = \frac{(C_i - C_e)}{C_i} \times 100 \qquad (6)$$

Where q_e (mg/g) is the equilibrium adsorption capacity of Hg(II). C_i and C_e are the initial and equilibrium concentration (mg/L) of Hg(II) respectively, M is the adsorbent dosage (mg).
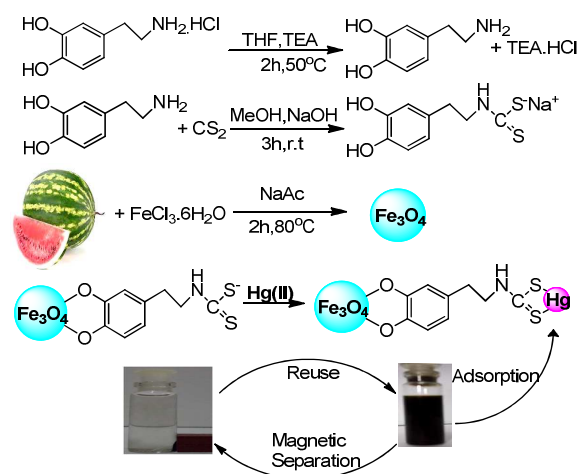

Scheme 1 Procedure for the synthesis of DHPCT and functionalized DHPCT@Fe_3O_4 MNPs for Hg(II) adsorption.

3. Results and discussion

3.1 Structure, morphology, and properties of DHPCT@Fe_3O_4 MNPs

The X-ray powder diffraction (XRPD) pattern of the DHPCT@Fe_3O_4 MNPs prepared using the watermelon rind extract is shown in Fig. 1. The XRPD pattern of the DHPCT@Fe_3O_4 MNPs was characterized by six strong diffraction peaks in the 2θ region of 10–70°. All of the diffraction peaks (i.e., at (111), (220), (311), (222), (400) and (440)) could be indexed to the cubic inverse spinel structure of DHPCT@Fe_3O_4 MNPs (JCPDS Card No. 89-0951) based on the diffraction peak positions and relative intensities. Thus, the formation of Fe_3O_4 MNPs in this study was confirmed.
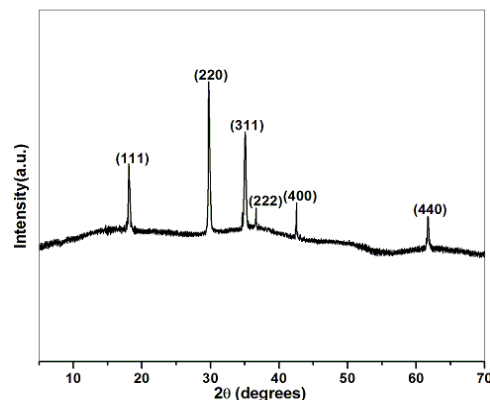
**Fig. 1** XRPD pattern of DHPCT@Fe_3O_4 MNPs.

This indicates that anchoring of DHPCT does not induce any phase change in the crystal structure of the Fe_3O_4 MNPs. The particle size was determined by applying the Scherrer equation (D = 0.89λ/βcosθ, where D is the average particle size, λ is the wavelength of the Cu-Kα irradiation, β is the intensity at the full width at half maximum of the diffraction peak, and θ is the diffraction angle for the (220) peak of the MNPs). The resulting mean crystallite size (13 nm) also coincides with the result

from TEM analysis. The results indicate that the DHPCT@Fe$_3$O$_4$ MNPs could be successfully prepared by an eco-friendly method.

FT-IR spectra were acquired to confirm functionalization of the surface of the Fe$_3$O$_4$ MNPs by DHPCT. The FT-IR spectrum of the watermelon rind extracts shows vibrational peaks at 3510, 2939, 1731, and 1695 cm^{-1}, corresponding to O–H stretching, C-H stretching, and vibration of the carbonyl and amide groups, respectively. The data indicate the presence of polyphenols in the extracts solution (Fig. 2a).[39] The polyphenol peaks in the IR spectrum of Fe$_3$O$_4$ prepared by using watermelon rind extract were shifted, from 3510 cm^{-1} to 3398 cm^{-1}. In addition, the peak shifted from 1731 to 1709 cm^{-1} was assigned C=O vibration of aldehyde derivatives, which demonstrates the role of biomolecules in the formation of Fe$_3$O$_4$ MNPs. The characteristic peak of Fe-O at 586 cm^{-1} proves the formation of the Fe$_3$O$_4$ MNPs (Fig. 2b). FT-IR peaks at 3355 and 3224 cm^{-1} correspond to the O-H groups of catechol and the -NH groups of secondary amine of DHPCT (Fig. 2c). Notably, the presence of the C=S stretching peak at 1073 cm^{-1} indicates the attachment of DHPCT on the surface of the Fe$_3$O$_4$ MNPs (Fig. 2d). Finally, it is found that IR peak corresponding to the CS$_2$ functional group shifted from 1073 to 1065 cm^{-1} after Hg(II) adsorption on DHPCT@Fe$_3$O$_4$ MNPs (Fig. 2e). The results clearly demonstrates the coordination of Hg(II) on the DHPCT ligand, which elucidate the Hg(II) removal mechanism using DHPCT@Fe$_3$O$_4$ MNPs (Scheme 1).
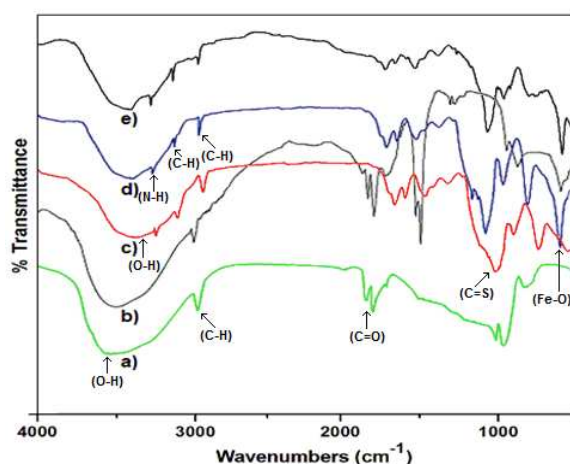
Fig. 2 FTIR spectra of (a) watermelon rind extract, (b) Fe$_3$O$_4$ MNPs, (c) DHPCT, and (d) DHPCT@Fe$_3$O$_4$ MNPs (e) DHPCT@Fe$_3$O$_4$ MNPs after Hg(II) adsorption.

The Raman spectra of Fe$_3$O$_4$ MNP and the DHPCT-capped Fe$_3$O$_4$ MNPs produced by green synthesis are shown in Fig. 3. The broad band observed at 669 cm^{-1} is assigned to the A$_{1g}$ modes of Fe$_3$O$_4$.[46] In addition, bands were apparent at 538 (T$_{2g}$), 306 (E$_g$), and 194 cm^{-1} (T$_{2g}$); these bands are characteristic of Fe$_3$O$_4$ MNPs (Fig. 3a).[47] No other characteristic iron oxide bands such as those of hematite (α-Fe$_2$O$_3$) or maghemite (γ-Fe$_2$O$_3$) were observed in the Raman spectra. DHPCT-capped MNPs showed a unique Raman band at 654 cm^{-1} (v_1) corresponding to a vibration mode of CS$_2$ (green circle),

which clearly demonstrates the presence of DHPCT on the surface of Fe$_3$O$_4$.
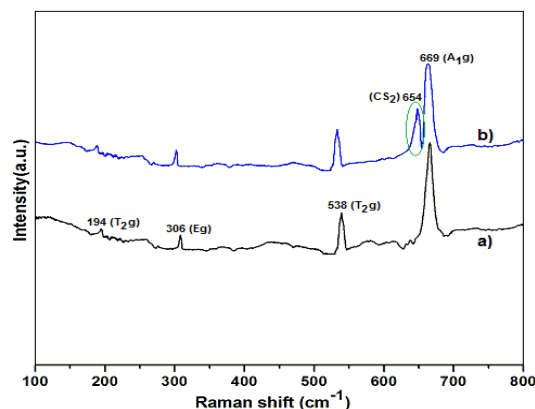
Fig. 3 Raman spectrum of (a) Fe$_3$O$_4$ MNPs and (b) DHPCT@Fe$_3$O$_4$ MNPs.

To further analyze the surface composition and structure of DHPCT@Fe$_3$O$_4$ MNPs X-ray photoelectron spectrometry (XPS) was carried out (Fig. 4). Wide range XPS of DHPCT@Fe$_3$O$_4$ MNPs clearly showed three dominant peaks at 284 eV, 530 eV, and 710/724 eV corresponding to C 1s, O 1s, and Fe 2p, respectively. In addition, small peaks for S 2p (169 eV), S 2s (226 eV) and N 1s (400 eV) are also presented, demonstrating the presence of DHPCT on the surface of the material. For careful analysis of Fe$_3$O$_4$ structure, a high-resolution spectrum of the Fe 2p is also presented (Fig. 4 inset). The peaks at 710.8 and 724.5 eV which are related to Fe 2p$_{3/2}$ and Fe 2p$_{1/2}$ respectively, confirming the formation of inverse spinel Fe$_3$O$_4$. No peak at 719 eV, which is the characteristic feature of Fe^{3+} ions in γ-Fe$_2$O$_3$, clearly confirmed the phase purity of DHPCT@Fe$_3$O$_4$ MNPs. By combining XRD, FT-IR, Raman, and XPS data, therefore, we can clearly confirm the formation of DHPCT@Fe$_3$O$_4$ by surface modification of biogenic Fe$_3$O$_4$ by DHPCT.
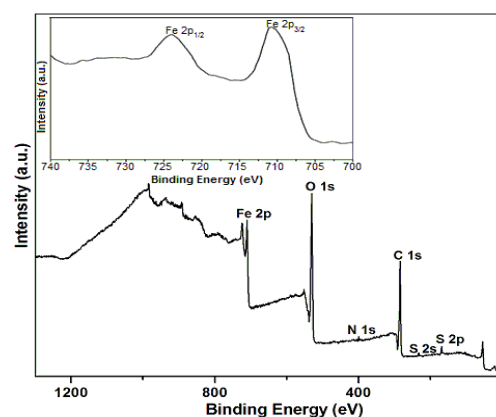
Fig. 4 XPS spectrum of DHPCT@Fe$_3$O$_4$ MNPs (inset shows high resolution scan of Fe 2p peaks of Fe$_3$O$_4$ MNPs).

Further compositional analysis of the DHPCT@Fe$_3$O$_4$ MNPs was carried out using TGA. The TGA data of Fe$_3$O$_4$ (Fig. 5a)

showed no significant weight loss above 150 °C, indicating the free state of the organic molecules of the Fe_3O_4 MNPs. However, the TGA data for the DHPCT@Fe_3O_4 MNPs (Fig. 5b) showed two independent weight loss steps; the first step at 100–150 °C corresponds to loss of adsorbed water molecules and the second step in the range of 150–285 °C indicates the presence of organic molecules, which may correspond to loss of the DHPCT ligand as a result of anchoring of the O-H groups (DHPCT) to the surface of the Fe_3O_4 MNPs. Therefore, it is concluded that the decomposition of DHPCT contributed to the second weight loss step observed in the TGA profile of the DHPCT@Fe_3O_4 MNPs. Furthermore, the observed weight loss suggests that the weight percentage of DHPCT in the DHPCT@Fe_3O_4 MNPs is around 14.5%.
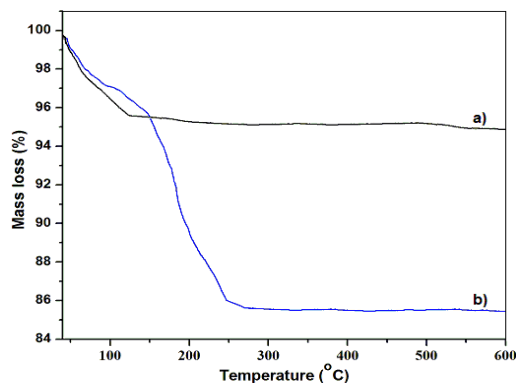

Fig. 5 TGA plots of (a) Fe_3O_4 MNPs and (b) DHPCT@Fe_3O_4 MNPs.

The morphology and size of the Fe_3O_4 nanoparticles in the DHPCT@Fe_3O_4 MNPs were observed *via* TEM. The TEM image (Fig. 6a) indicated the presence of spherical nanoparticles. The size of the majority of particles was below 17 nm, and the particles were agglomerated due to the presence of hydroxyl groups from the extract. Fig. 6b presents the particle size histogram for the freshly prepared DHPCT@Fe_3O_4 MNPs, indicating a mean diameter of 5 - 20 nm. The selected area diffraction (SAED) image (Fig. 7, upper inset) displays diffraction spots of poly-crystalline species; these patterns correspond to the (111), (220), and (311) indices of Fe_3O_4 with the inverse spinel structure. The chemical composition analysis of the DHBPCT@Fe_3O_4 nano-composite by EDS clearly showed the presence of S, Fe, and O (Fig. 7). The TEM image and EDS data proved the presence of Fe_3O_4 nanoparticles with a size of 17 nm capped with the sulfur containing ligand (DHPCT).
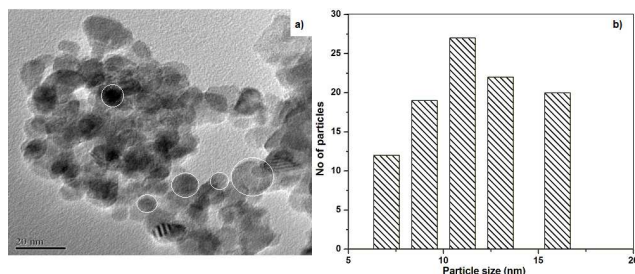

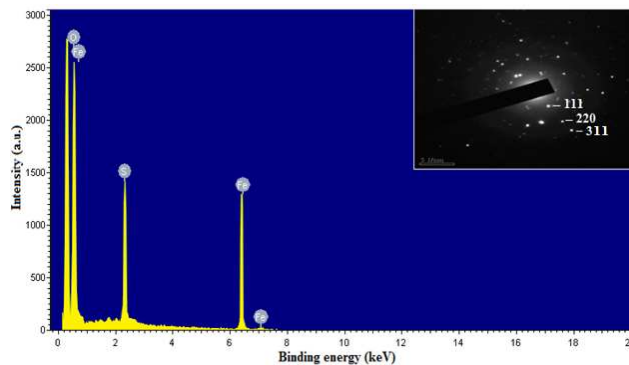**Fig. 6** TEM image of (a) DHPCT@Fe_3O_4 MNPs and (b) particle size histogram.

Fig. 7 EDS spectrum and SAED pattern (inset) of DHPCT@Fe_3O_4 MNPs.

The surface area and pore size distribution of the prepared DHPCT@Fe_3O_4 MNPs were calculated from the N_2 adsorption-desorption isotherm data acquired at 77 K (Fig. 8). The Brunauer-Emmett-Teller (BET) surface area of the DHPCT@Fe_3O_4 MNPs calculated from the N_2 adsorption isotherm was 9.58 m^2/g with a pore volume of 0.996 cm^3/g. The pore size distribution was obtained from adsorption isotherm analysis *via* the Barrett-Joyner-Halenda (BJH) method (Fig. 8, inset), which indicates that most of the pores have a size of ~2 nm (random macropores with sizes above 50 nm are also presented). The N_2 adsorption isotherm data clearly demonstrate the porosity of the resulting material, which should prove advantageous for the removal of Hg(II) by providing an increased contact area. In addition, the mesoporosity of the resulting material should facilitate diffusion of hydrated mercury ions through the porous composite material.
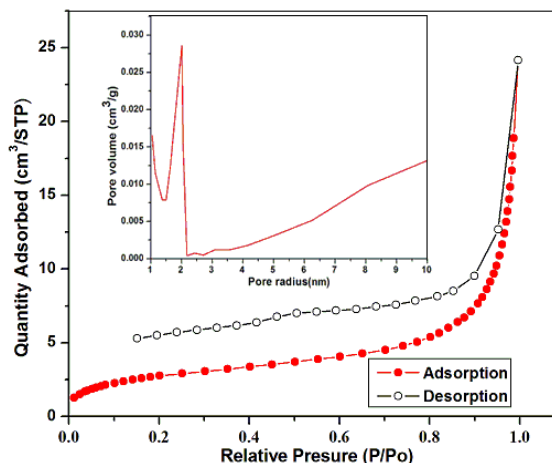

Fig. 8 N_2 adsorption desorption isotherm (at 77 K) and pore size distribution (inset) of DHPCT@Fe_3O_4 MNPs.

3.2 Parameters affecting Hg(II) adsorption (pH, adsorbent dosage and initial concentration)

The pH of the solution is one of the most important parameters affecting Hg(II) adsorption. The effect of pH on the removal of Hg(II) ions by the Fe_3O_4-based materials before and

after capping was investigated within the pH range of 2 - 9 at 303 K with variation of the initial Hg(II) concentration (20, 40, and 60 mg/L). The amount of Hg(II) removed from the solution increased as the pH increased within the range of 2 - 7, followed by a decline in the Hg(II) removal above pH 7. The maximum Hg(II) removal achieved with the DHPCT-capped nano-composite was 97.8% at pH 7.0 using an initial Hg(II) concentration of 60 mg/L (Fig. 9). Formation of a colloidal precipitate of $Hg(OH)^+$, $Hg(OH)_2$, $Hg(OH)_3^-$ at high pH may account for the decline in the Hg(II) removal at high pH values (pH > 7).[50] In addition, the metal-binding ability of the CS_2^- functional group in DHPCT changes depending on the concentration of hydrogen (H^+) ions (pH value) in the solution due to protonation of the CS_2^- functional group. At high H^+ concentration (or at low pH), the CS_2^- functional group can be further protonated to form $CS_2H_2^+$ (Eq. 8), thereby preventing coordination of Hg(II) because of electrostatic repulsion between the positive charges. Therefore, the pH dependent Hg(II) removal capacity of the DHPCT@Fe$_3$O$_4$ MNPs can be explained. The initial Hg(II) concentration also affects the Hg(II) removal efficiency. Three different concentrations (20, 40, and 60 mg/L) were assessed in the study of the effect of the initial Hg(II) concentration, demonstrating that the mercury removal efficiency increased with increasing initial concentration. For all initial concentrations, the mercury removal efficiency reached a maximum at pH 7 and decreased with any further increase or decrease of the pH values. Finally, the effect of DHPCT capping on the Hg(II) removal was analyzed by comparing the Hg(II) removal efficiency of Fe$_3$O$_4$ (black triangle) and DHPCT@Fe$_3$O$_4$ (green triangle) (initial concentration: 60 mg/L for both). Without DHPCT capping, the Hg(II) removal efficiency of the Fe$_3$O$_4$ MNPs was very low (35%), whereas almost complete removal of Hg(II) from 60 mg/L solution (98%) was achieved with DHPCT-capped Fe$_3$O$_4$, suggesting that introduction of the DHPCT functional group is crucial for the removal of Hg(II). Therefore, it was concluded that optimal mercury removal can be achieved when the initial Hg(II) concentration is 60 ml/g using the DHPCT capped Fe$_3$O$_4$ MNPs at pH 7.
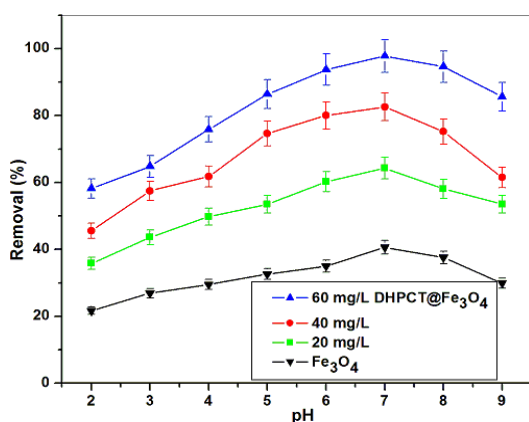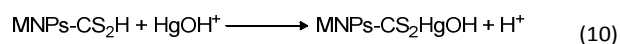

Fig. 9 Influence of pH on Hg(II) adsorption by DHPCT@Fe$_3$O$_4$ MNPs at 303 K with different initial metal ion concentrations.

Evaluation of the pH dependence of the Hg(II) adsorption efficiency provides insight into the Hg(II) adsorption mechanism. Protonation of the CS_2^- functional group at low pH can produce a neutral or positive charge on the DHPCT ligand (Eqs. 7, 8). Mercuric species (Hg(II), $Hg(OH)^+$, or $Hg(OH)_2$) can coordinate to the neutral CS_2H functional group (Eqs. 9 - 11) resulting in a neutral complex (MNPs-CS_2HgOH). Therefore, it is expected that the change in the mercury adsorption with pH can be explained based on the following mechanism (Eqs. 7 - 11).

$$\text{MNPs-CS}_2^- + \text{H}^+ \longrightarrow \text{MNPs-CS}_2\text{H} \qquad (7)$$

$$\text{MNPs-CS}_2\text{H} + \text{H}^+ \longrightarrow \text{MNPs-CS}_2\text{H}_2^+ \qquad (8)$$

$$\text{MNPs-CS}_2\text{H} + \text{Hg}^{2+} \longrightarrow \text{MNPs-CS}_2\text{Hg}^+ + \text{H}^+ \qquad (9)$$

$$\text{MNPs-CS}_2\text{H} + \text{HgOH}^+ \longrightarrow \text{MNPs-CS}_2\text{HgOH} + \text{H}^+ \qquad (10)$$

$$\text{MNPs-CS}_2\text{H} + \text{Hg(OH)}_2 \longrightarrow \text{MNPs-CS}_2\text{HgOH} + \text{H}_2\text{O} \qquad (11)$$

3.3 Adsorption kinetic studies and sorption capacity analysis

The effect of the duration of contact with the DHPCT@Fe$_3$O$_4$ MNPs on the adsorption of Hg(II) was also studied to understand the adsorption kinetics (Fig. 10). The following experimental conditions were employed for determination of the adsorption amount depending on time: 60 mg/L concentration solution, pH 7, room temperature, and 2.5 mg of the composite for 25 ml of solution. The adsorption processes proceeded rapidly and reached the adsorption equilibrium in 60 min.
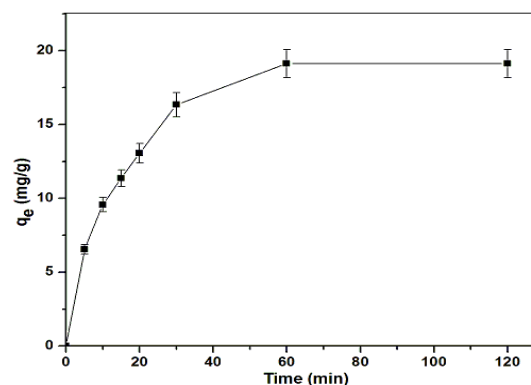

Fig. 10 Dependence of Hg(II) adsorption capacity of DHPCT@Fe$_3$O$_4$ MNPs on contact time.

The pseudo-first-order[51] and pseudo-second-order[52] kinetic models were employed to study the kinetics of Hg(II) removal using the prepared magnetic nano-composites. When the pseudo-first-order kinetic model was applied to the adsorption data, the results did not fit well to the pseudo-first-order kinetic model as shown in Fig. S1 and Table S1 (See ESI). However, application of the pseudo-second-order kinetic model for analysis of the sorption kinetics (Eq. 12) produced a good linear fit (R^2 = 0.9996) (Fig. 11 and Table S1). Therefore,

Please do not adjust margins

the adsorption system obeyed pseudo-second-order kinetics for the entire adsorption period, suggesting that Hg(II) adsorption proceeded mainly *via* chemisorption.[53]

$$\frac{t}{q_t} = \frac{1}{k_2 q_e^2} + \left(\frac{1}{q_e}\right) t \qquad (12)$$

Where k_2 (g/mg min^{-1}) is the pseudo-second-order rate constant, q_e (mg/g) and q_t (mg/g) are the amount of Hg(II) adsorbed at equilibrium and at time t, respectively. The values of k_2 and q_e can be calculated from the slope and intercept of a plot of t/q_t vs. t.
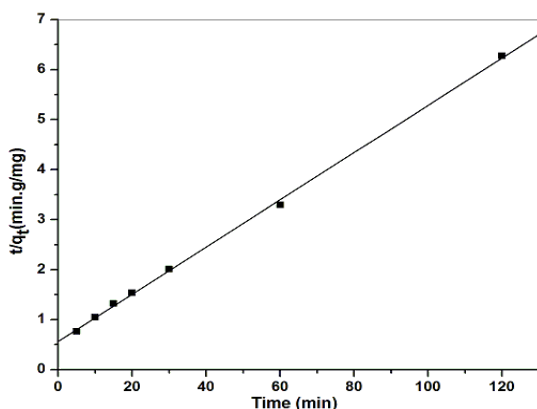

Fig. 11 Pseudo second-order kinetics of Hg(II) adsorption on DHPCT@Fe$_3$O$_4$ MNPs.

To evaluate the maximum capacity and equilibrium of Hg(II) adsorption by DHPCT@Fe$_3$O$_4$ MNPs, the Hg(II) adsorption data were analyzed using the Langmuir and Freundlich isotherm models. The Langmuir equation (Eq. 13) can be expressed by the linearized form:

$$\frac{C_e}{q_e} = \frac{C_e}{q_m} + \frac{1}{q_e b} \qquad (13)$$

Where q_e is the equilibrium concentration of metal ions on the adsorbent (mg/g), C_e is the equilibrium concentration of metal ions in the solution (mg/L), q_m is the maximum adsorption capacity of the adsorbent (mg/g), and b (L/mg) is the equilibrium constant relating to the sorption energy.
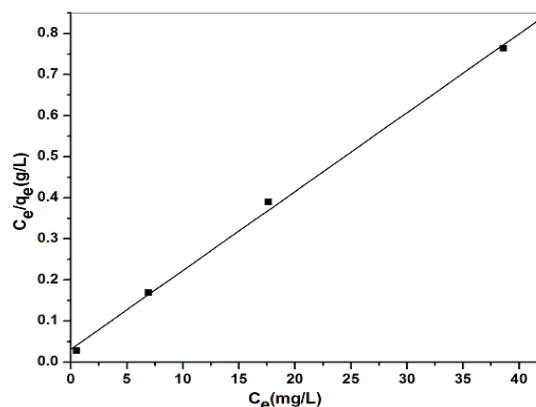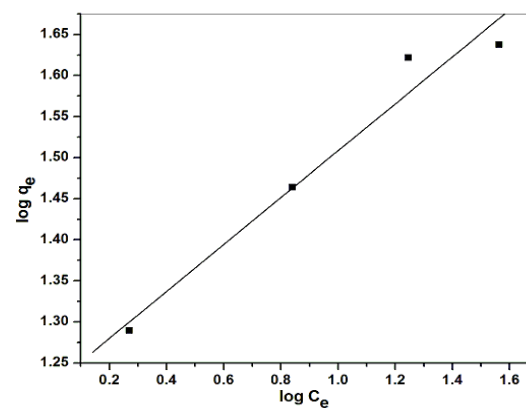

Fig. 12 Fit of data for Hg(II) sorption on DHPCT@Fe$_3$O$_4$ MNPs to Langmuir isotherm.

The Langmuir adsorption model (solid line) produced a good linear fit of the experimental Hg(II) adsorption data (square symbols) (Fig. 12). The maximum Hg(II) adsorption capacity calculated from the fitted plot was 52.1 mg/g. Further calculated parameters are presented in Table S2 (See ESI). In addition, another parameter in the Langmuir adsorption isotherm, a dimensionless factor (R_L), is described in Eq. 14. For favorable sorption, R_L should be between 0 and 1, whereas a R_L value of more than 1 indicates unfavorable sorption. In this study, the calculated R_L value was 0.0063, indicating favorable adsorption of Hg(II) on the DHPCT@Fe$_3$O$_4$ MNPs.

$$R_L = \frac{1}{1 + bC_i} \qquad (14)$$

Where C_o (mg/g) is initial metal concentration and b (L/mg) is the Langmuir constant.

Fig. 13 Fit of data for Hg(II) sorption on DHPCT@Fe$_3$O$_4$ MNPs to Freundlich isotherm.

The Freundlich isotherm model can also be used to fit the data for Hg(II) adsorption on heterogeneous surfaces (Eq. 15). The experimental adsorption data (square symbols) for the DHPCT@Fe$_3$O$_4$ MNPs at 303 K fitted well to the Freundlich isotherm model with a R^2 value of 0.9809 (Fig. 13). The constant n in the Freundlich equation provides insight into the

un/favorability of the Hg(II) adsorption process. When the calculated *n* value is larger than 1, the adsorption process can be considered favorable.[54, 55] The *n* value calculated from the fitted data was 3.50, and thus the Hg(II) adsorption process using the DHPCT@Fe_3O_4 MNPs can be considered as a favorable process. Finally, the Hg(II) adsorption capacity of other reported adsorbents and that of DHPCT@Fe_3O_4 MNPs calculated using the Langmuir isotherm model are summarized in Table 1.[56-61] It should be noted that superior results were achieved with the prepared material compared to the other reported materials.

$$\log q_e = \log k_f + \frac{1}{n} \log C_e \qquad (15)$$

Where k_f (mg/g) and *n* are the Freundlich isotherm constants that represent the adsorption and the intensity of adsorbents.

Table 1 Adsorption capacities of various adsorbents for Hg(II) removal from water

| Type of adsorbent	Capacity (mg/g)	Reference
Activated carbon	25.8	56
Dithiocarbamate@mesoporous SiO_2	40.1	57
Graphene oxide/Fe_3O_4	18.2	58
Thioacetamide@SiO_2	17.5	59
Camel bone charcoal	28.2	60
SH-Fe_3O_4-NMPs[62]	125-256	61
DHPCT@Fe_3O_4 MNPs	52.1	This work

3.4 Adsorption selectivity

In the case of metal ion removal by coordination, the co-existing heavy metal ions often reduce the sorption capacity *via* the competing effect. The influence of other metal ions for the adsorption of Hg(II) was investigated. A mixed solution of metal ions containing Pb(II), Ni(II), Cu(II), Co(II) and Zn(II) was prepared, concentrations of all the heavy metal ions set at ~60 mg/L. The adsorption of Hg(II) sorption efficiency from the mixed metal ion solution using DHPCT@Fe_3O_4 MNPs was more than 96% even in the presence of various competing ions, which is similar to the adsorption experiment using pure Hg(II) ion solution. The composite shows much higher removal efficiency for Hg(II) ions than the other metal ions in an order of Hg(II) >> Co(II) > Zn(II) > Cu(II) > Pb(II) > Ni(II) (Fig. 14). It is expected that carbamodithioate (CS_2^-) functional group plays a crucial role in the Hg(II)-selectivity due to softness of the base. This result clearly suggests selective sorption of Hg(II) onto the DHPCT@Fe_3O_4 MNPs surface without interference from the other metal ions (See ESI for experimental details).
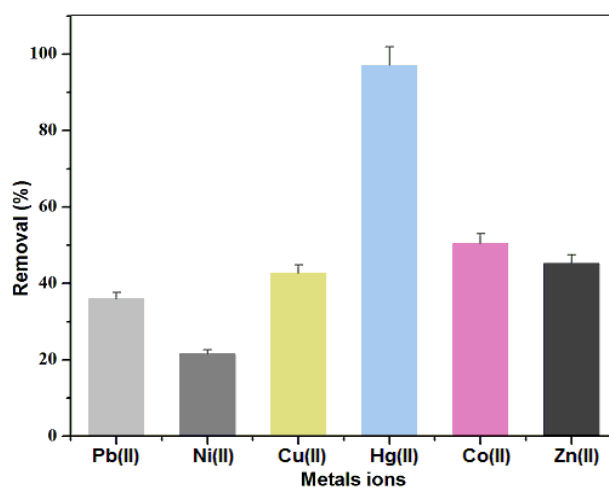
Fig. 14 Hg(II) removal from the mixed solution of heavy metal ions(Pb(II), Ni(II), Cu(II), Co(II), and Zn(II)) using DHPCT@Fe_3O_4 MNPs.
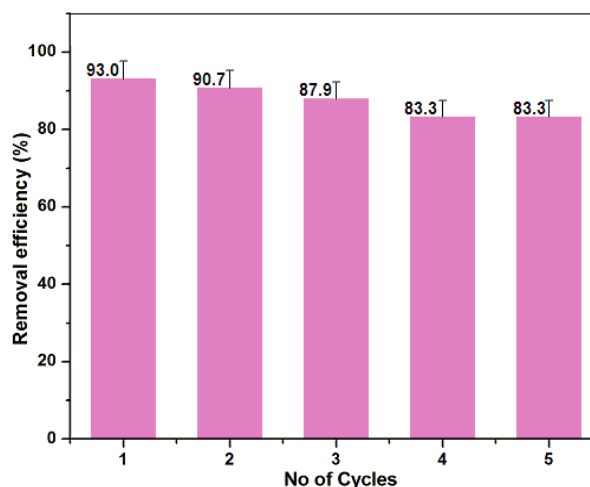
3.5 Magnetic property analysis

The magnetic character of the Fe_3O_4 and DHPCT@Fe_3O_4 MNPs was demonstrated by examining the magnetic hysteresis loops at room temperature (Fig. 15). Magnetization of the prepared materials resulted in unique hysteresis loops corresponding to ferromagnetic behavior of Fe_3O_4 and the DHPCT@Fe_3O_4 MNPs with a saturation magnetization (M_s) value of 28.4 emu/g and 24.7 emu/g for Fe_3O_4 and the DHPCT@Fe_3O_4 MNPs, respectively. The lower saturation magnetization of the DHPCT-capped nano-composite relative to that of Fe_3O_4 is due to the quenching of the magnetic moment by the interaction between the coated DHPCT and Fe_3O_4 MNPs. The expanded hysteresis loops obtained at field strengths between -2 kG and 2 kG demonstrate the ferromagnetic character of the Fe_3O_4 MNP and DHPCT@Fe_3O_4 MNP composites (Fig.15, left inset). The results showed nonzero remnant magnetization (M_r) and coercive force (H_c) with a non-linear hysteresis loop, which also revealed the ferromagnetic character of the resulting materials.[63] Separation of DHPCT@Fe_3O_4 from the medium by sedimentation of the MNPs requires a duration of 30 min for settling of the particles. However, it takes just 15 seconds to remove the MNPs by using an external magnet (right inset in Fig. 15). The rapid isolation of the DHPCT@Fe_3O_4 MNPs using an external magnetic field may allow good recyclability for Hg(II) removal application.

Journal Name

ARTICLE
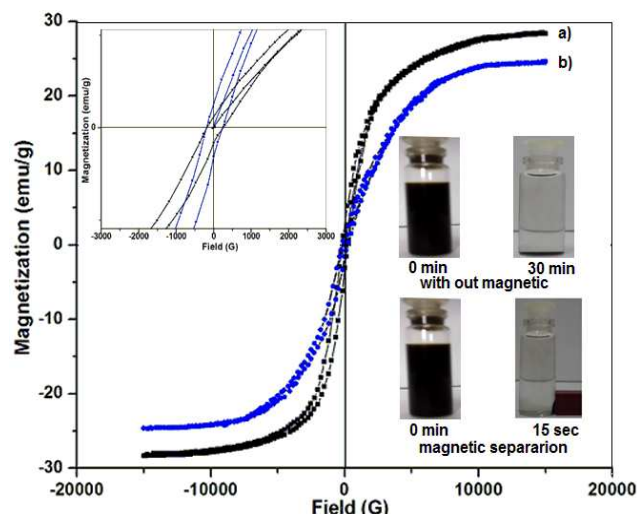
Fig. 15 Magnetization curves of (a) Fe$_3$O$_4$ MNPs and (b) DHPCT@Fe$_3$O$_4$ MNPs (right inset: separation of DHPCT@Fe$_3$O$_4$ MNPs from water).

Fig. 16 Recycling efficiency of DHPCT@Fe$_3$O$_4$ MNPs for Hg(II) adsorption during cyclic experiments (MNPs concentration: 0.1 g/L at pH 7.0).

3.6 Recyclability test

Due to the recent drive towards environmental sustainability and economic efficiency, recycling of the DHPCT@Fe$_3$O$_4$ MNPs in the removal of Hg(II) was studied. From the pH study, it was found that the amount of Hg(II) adsorbed decreased at low pH, and thus acidic medium was used for regeneration of the Hg(II)-loaded DHPCT@Fe$_3$O$_4$ MNPs. Following the adsorption experiment, regeneration of the DHPCT@Fe$_3$O$_4$ MNPs by Hg(II) desorption was carried out by washing the adsorbent with an acidic solution (HNO$_3$, pH ~ 2) followed by further rinsing with deionized water. The washed DHPCT@Fe$_3$O$_4$ MNPs were dried at 95 °C for reuse. In successive experiments using the recycled material, the Hg(II) removal capacity declined slightly from 93.0 to 90.7, 87.9 and 83.3%. However, the removal efficiency was higher than 80% even after five Hg(II) removal cycles (Fig. 16). The slight decrease in the Hg(II) removal efficiency may be due to loss of the DHPCT ligand by treatment with the acidic solution during the regeneration processes. A milder regeneration process may be helpful to increase the recyclability of the composite material. Finally, the results lead to the conclusion that the DHPCT@Fe$_3$O$_4$ MNPs have great adsorption capacity and are also potentially highly useful for decontamination of water by removal of toxic metals.

Conclusions

In this work, Fe$_3$O$_4$ magnetic nanoparticles were successfully prepared by a green synthetic process using a fruit waste (watermelon rind extract) without using a chemical surfactant and reducing agent. The prepared Fe$_3$O$_4$ was further capped by the DHPCT ligand *via* a facile synthetic method, and the composite was applied to the removal of Hg(II) from aqueous solution. Surface characterization of the DHPCT@Fe$_3$O$_4$ MNPs was successfully performed using XRPD, FT-IR, Raman spectroscopy, and TGA. The mesoporosity of the resulting composite with 2 nm pore size was demonstrated by N$_2$ adsorption analysis. Several parameters affecting Hg(II) removal, including the pH, initial Hg(II) concentration, and DHPCT capping, were investigated. Notably, it was found that the soft ligand (DHPCT) that can coordinate with the soft metal ion (Hg(II)) plays a vital and preferential role for the selective mercury removal. The maximum mercury adsorption capacity of DHPCT@Fe$_3$O$_4$ was 52.1 mg/g at room temperature, at neutral pH, which is one of the best results reported for heterogeneous adsorbents geared towards Hg(II) removal. Moreover, the ferromagnetic character of the Fe$_3$O$_4$ MNPs facilitates simple removal of the adsorbent from the medium by applying an external magnet; the recovered material can be recycled at least 5 times while maintaining more than 80% Hg(II) removal efficiency. To the best of our knowledge, this is the first example of Fe$_3$O$_4$ MNPs synthesis using watermelon rind extract, leading to the high Hg(II) adsorption capacity after DHPCT incorporation among the reported Hg(II) adsorbents. Therefore, we expect that this finding may provide new insight into the design and tailoring of high performance Hg(II) adsorbents by an eco-friendly method.

Acknowledgements

Notes and references

1   P. D. Armitage, M. J. Bowes, H. M. Vincent, *River Res. Appl.*, 2007, **23**, 997–1015.
2   S. Islam, K. Ahmed, R. Mohammad, H. Mamun, K. Islam, *Ecological Indicators* 2015, **48**, 282–291.
3   P. Holmes, K. A. F. James, L. S Levy, *Sci. Total Environ.*, 2009, **408**, 171–182.
4   A. Mousavi, R. D. Chavez, A. M. S. Ali, S. E. Cabaniss, *Environ. Forensics.*, 2011, **12**, 14–18.
5   R. S. Vieira, M. M. Beppu, *Water Res.*, 2006, **40**, 1726–1734.
6   F. Zahir, S. J. Rizwi, S. K. Haq, R. H. Khan, *Toxicol. Pharmacol.*, 2005, **20**, 351–360.
7   P. Grandjean, H. Satoh, K. Murata, K. Eto, *Environ. Health Perspect.*, 2010, **118**, 1137–1145.
8   Q. R. Wang, D. Kim, D. D. Dionysiou, G. A. Sorial, D. Timberlake, *Environ. Pollut.*, 2004, **131**, 323–336.
9   P. Huttenloch, K. E. Roehl, K. Czurda, *Environ. Sci. Technol.*, 2003, **37**, 4269–4273.
10 W. S. Wan Ngah, L. C. Teonga, M. A. K. M. Hanafiah, *Carbohy Polym.*, 2011, **83**, 1446–1456.
11 A. Oehmen, R. Viegas, S. Velizarov, M. A. M. Reis, J. G. Crespo, *Desalination*, 2006, **199**, 405–407.
12 N. J. O Driscoll, S. D. Siciliano, D. R. S. Lean, M. Amyot, *Environ. Sci. Technol.*, 2006, **40**, 837–843.
13 N. Pourreza, K. Ghanemi, *J. Hazard. Mater.*, 2009, **161**, 982–987.
14 S. M. Evangelista, E. Deoliveira, G. R. Castro, L. F. Zara, A. G. S. Prado, *Surf. Sci.*, 2007, **601**, 2194–2202.
15 K. M. Dilip, K. N. Barun, M. K. Purkait, *J. Environ. Chem. Eng.*, 2013, **1**, 891–898.
16 H. G. Park, T. W. Kim, M. Y. Chae, I. K. Yoo, *Process Biochem.*, 2007, 42, 1371–1377.
17 S. P. Bayen, P. Chowdhury, *J. Environ. Chem. Eng.*, 2015, **3**, 70–78.
18 L. Carro, J. L. Barriada, R. Herrero, M E. S. De Vicente, *Chem. Eng. J.*, 2013, **229**, 378–387.
19 B. Dou, H. Chen, *Desalination,* 2011, **269**, 260–265.
20 C. Ray, S. Sarkar, S. Dutta, A. Roy, R. Sahoo, Y. Negishi, T. Pal, *RSC Adv.*, 2015, **5**, 12446–12453.
21 Z. Qu, L. Yan, L. Li, J. Xu, M. Liu, Z. Li, N. Yan, *ACS Appl. Mater. Interfaces,* 2014, **6**, 18026–18032.
22 L. Sun, Y. Li, M. Sun, H. Wang, S. Xu, C. Zhang, Q. Yang, *New J. Chem.*, 2011, **35**, 2697–2704.
23 C. Chappert, A. Fert, F. N. Van Dau, *Nat. Mater.*, 2007, **6**, 813–823.
24 Y. Zhu, T. Ikoma, N. Hanagata, S. Kaskel, *Small,* 2010, **6**, 471–478.
25 M. Ojeda, A. M. Balu, V. Barron, A. Pineda, A. Garcia, A. A. Romero, R. Luque, *J. Mater. Chem. A,* 2014, **2**, 387–393.
26 C. S. Kumar, F. Mohammad, *Drug Delivery Rev.*, 2011, **63**, 789–808.
27 E. J. Kim, C. S. Lee, Y. Y. Chang, Y. S. Chang, *ACS Appl. Mater. Interfaces,* 2013, **5**, 9628–9634.
28 Y. Wang, B. Zou, T. Gao, X. Wu, S. Lou, S. Zhou, *J. Mater. Chem.*, 2012, **22**, 9034–9040.
29 Z. Limin, L. Zhirong, L. Jinhui, H. Qunwu, *Desalination,* 2010, **258**, 41–47.
30 T. Tanaka, R.Sakai, R. Kobayashi, K. Hatakeyama, T. Matsunaga, *Langmuir,* 2009, **25**, 2956–2961.
31 S. Yin, Z. Luo, J. Xia, H. Li, *J. Phys. Chem. Solids,* 2010, **71**, 1785–1788.

32 G. Davood, S. N. Masoud, G. K. Majid, *J. Ind. Eng. Chem.,* 2014, **20**, 3970–3974.
33 M. Abbas, B. P. Rao, M. O. A. Hamed, C. G. Kim, *J. Alloys and Comp.,* 2014, **615**, S308–S312.
34 S. Li, W. Zhang, F. Chen, R. Chen, *Mater. Res. Bull.,* 2015, **66**,186–191.
35 M. Anbarasu, M. Anandan, E. Chinnasamy, V. Gopinath, K. Balamurugan, *Spectrochim. Acta A,* 2015, **135**, 536–539.
36 Y. Cai, Y. Shen, A. Xie, S. Li, X. Wang, *J. Magn. Magn. Mater.,* 2010, **322**, 2938–2943.
37 S. Venkateswarlu, Y. SubbaRao, T. Balaji, B. Prathima, N. V. V. Jyothi, *Mater. Lett.,* 2013, **100**, 241–244.
38 Y. Parka, S. Cho, *Israel J. Plant Sci.,* 2012, **60**, 415–423.
39 A. M. Rimandoa, P. M. P. Veazie, *J. Chromatogr. A,* 2005, **1078**,196–200.
40 A. Mort, Y. Zheng, F. Qiu, M. Nimtzc, G. Bell-Eunice, *Carbohydr. Res.,* 2008, **343**, 1212–1221.
41 G. Z. Memon, M. I. Bhanger, M. Akhtar, F. N. Talpur, J. R. Memon, *Chem. Eng. J.,* 2008, **138**, 616–621.
42 N. A. Reddy, R. Lakshmipathy, N. C. Sarada, *Alexandria Eng. J.,* 2014, **53**, 969–975.
43 R. G. Pearson, *J. Am. Chem. Soc.,* 1963, **85**, 3533–3539.
44 R. Say, E. Birlik, Z. Erdemgil, A. Denizli, A. Ersoz, *J. Hazard. Mater.,* 2008, **150**, 560–564.
45 S. H. Liu, R. M. Xing, F. Lu, R. K. Rana, J. J. Zhu, *J. Phys. Chem. C,* 2009, **113**, 21042–21047.
46 O. N. Shebanova P. Lazor, *J. Solid State Chem.,* ,2003, **174**, 424 - 430.
47 L. Slavov, M. V. Abrashev, T. Merodiiska, Ch. Gelev, R. E. Vandenberghe, I. M. Deneva, I. Nedkov, *J. Magn. Magn. Mater.,* 2010, **322**,1904–1911.
48 M. Liu, T. Wen, X. Wu, C. Chen, J. Hu, J. Li, X. Wang, *Dalton Trans.,* 2013, **42**, 14710–14717.
49 S. Zheng, P. Han, Z. Han, H. Zhang, Z. Tang, J. Yang, *Sci. Report,* 2014, **4**, 4842–4848.
50 Y. Inoue, M. Munemori, *Environ. Sci. Technol.,* 1979, **13**, 443–445.
51 Z. Y. Yao, J. H. Qi, L. H. Wang, *J. Hazard. Mater.,* 2010, **174**, 137–143.
52 Y. S. Ho, G. Mckay, *Process Biochem.,* 1999, **34**, 451–465.
53 G. Crini, H. N. Peindy, F. Gimbert, C. Robert, *Sep. Purif. Technol.,* 2007, **53**, 97–110.
54 B. H. Hameed, D. K. Mahmoud, A. L. Ahmad, *J. Hazard. Mater.,* 2008, **158**, 65–67.
55 J. Gong, T. Liu, X. Wang, X. Hu, L. Zhang, *Environ. Sci. Technol.,* 2011, **45**, 6181–6187.
56 M. M. Rao, D. Reddy, P. Venkateswarlu, K. Seshaiah, *J. Environ. Manage.,* 2009, **90**, 634–643.
57 K. A. Venkatesan, T. G. Srinivasan, P. R. V. Rao, *J. Radioanal. Nucl. Ch.,* 2003, **256**, 213–218.
58 J. Li, S. Zhang, C. Chen, G. Zhao, X. Yang, J. Li, X. Wang, *ACS Appl. Mater. Interfaces,* 2012, **4**, 4991–5000.
59 S. P. Bayen, P. Chowdhury, *J. Environ. Chem. Eng.,* 2015, **3**, 70–78.
60 S. S. M. Hassan, N. S. Awwad, A. H. A. Aboterika, *J. Hazard. Mater.,* 2008, **154**, 992–997.
61 S. Pan, Y. Zhang, Haoyu Shen, M. Hu, *Chem. Eng. J.,* 2012, **210**, 564–574.
62 Despite higher Hg^{2+} adsorption capacity of SH-Fe$_3$O$_4$-NMPs, the environmentally benign and cheap synthetic procedure and the higher magnetic saturation value of DHPCT@Fe$_3$O$_4$ MNPs may allow easier access to the material for a variety of applications.
63 S. Venkateswarlu, M. Yoon, *RSC Adv.,* 2015, **5**, 65444–65453.

Graphical Abstract

A new carbamodithioate based ligand (3,4-Dihydroxyphenethylcarbamodithioate, DHPCT)-capped biogenic Fe_3O_4 magnetic nanocomposite has been synthesized using watermelon rind extract for rapid removal of Hg(II) ions from water with a facile recyclability.